Analysis and Reduction of Radial Vibration of FSCW PMSM Considering the Phase of Radial, Tangential Forces, and Tooth Modulation Effect

Jae-Hyun Kim, *Member, IEEE*, Yun-Jae Won, and Myung-Seop Lim, *Senior Member, IEEE*

***Abstract*— In this study, the causes of significant radial vibration at pole frequency in an 18-slot 16-pole (18S16P) permanent magnet synchronous motor (PMSM) are thoroughly analyzed, and an improved model is proposed. First, the spatial phase relationship of the lowest order radial and tangential air-gap electromagnetic force densities (AEFDs) of the 18S16P PMSM is derived analytically. Then, using 3-D structural finite element analysis (FEA), the radial vibration-enhancing effect of the lowest order radial and tangential AEFDs is revealed. Furthermore, the tooth modulation effect of the 18S16P PMSM is investigated. The analysis results show that the modulated radial vibration is also enhanced by the radial vibration caused by the lowest order radial and tangential AEFDs, leading to significant pole-frequency radial vibrations. Afterward, a vibration reduction model is proposed to minimize the tooth modulation effect and utilize the vibration suppression effect caused by the lowest order radial and tangential AEFDs considering the spatial phase relationships. As a result, radial vibrations are greatly reduced, and the results are validated through simulations and tests.**

***Index Terms*— Air-gap electromagnetic force density (AEFD), tangential force, tooth modulation effect, vibration.**

I. Introduction

DUE to high power density, high efficiency, low cogging torque, low torque ripple, and excellent manufacturability, fractional-slot concentrated winding (FSCW) permanent magnet synchronous motors (PMSMs) are widely used in numerous applications, such as electric propulsion, servo systems, and home appliances [1], [2], [3], [4]. Consequently, the vibration characteristics of these motors are increasingly vital in such applications [5], [6], [7]. Although FSCW PMSMs offer several advantages, their pole-frequency vibration characteristics are inferior compared to those of distributed winding PMSMs, primarily because of the lower spatial harmonic order of their air-gap electromagnetic force density (AEFD) [8]. The radial displacement of the PMSM is inversely proportional to a quarter of the lowest spatial order of its AEFD. Consequently, increasing the lowest spatial order of the AEFD can substantially reduce the vibration of the PMSM [9]. The determination of the lowest spatial order of the AEFD is reliant on the pole–slot combination of the PMSM; hence, enhancing the vibration characteristics of FSCW PMSMs can be achieved by opting for a pole–slot combination with a larger lowest spatial order of the AEFD [10]. However, increasing the lowest spatial order of the AEFD typically nullifies several advantages of FSCW PMSMs. For instance, the fundamental winding factor decreases, and the harmonic winding factor increases, resulting in decreased power density and increased torque ripple. Consequently, methods to reduce vibrations without compromising the desirable attributes of FSCW PMSMs are imperative.

The dominant pole-frequency vibration in an FSCW PMSM is typically caused by the lowest spatial harmonic order radial AEFD. This lowest spatial order arises from the interaction between the fundamental component of the PM field and either the slotting effect or armature reaction, resulting in a generally significant amplitude. However, recently, in-depth studies on tangential AEFD and higher order radial AEFD have been widely conducted [11], [12], [13], [14], [15], [16], [17], [18], [19], [20]. In [11], it was noted that the effect of local tangential force on PMSM vibration is comparable to that of local radial force. In addition, Fang et al. [12] explored a tooth modulation effect, revealing that a high-order radial force behaves like a low-order radial force due to the tooth-slot structure, leading to substantial vibrations. Moreover, research on the impact of asymmetrical geometry on torque ripple and vibration [13], [14] showed that while torque ripple can be effectively reduced by employing an asymmetrically shaped rotor, vibrational characteristics worsen due to the tooth modulation effect. Similarly, the vibration of a bread-loaf PM was examined in [15], revealing that while the bread-loaf shape PM reduces the harmonic component of magnetic flux density, it increases PMSM vibration due to the tooth modulation effect. In [16], [17], the pole-frequency vibration of a surface-mounted PMSM was reduced by employing piecewise stagger-trapezoidal poles. However, only the concentrated radial and tangential forces were considered, without considering the concentrated moment. Finally, Zhu et al. [18] introduced a design for reducing pole-frequency vibration by

Manuscript received 8 March 2024; revised 6 June 2024; accepted 15 July 2024. Date of publication 22 July 2024; date of current version 3 February 2025. This work was supported by the 2024 Yeungnam University Research Grant. *(Corresponding author: Myung-Seop Lim.)*

Jae-Hyun Kim is with the Department of Mechanical Engineering, Yeungnam University, Gyeongbuk 38541, Republic of Korea (e-mail: jaehyun@yu.ac.kr).

Yun-Jae Won and Myung-Seop Lim are with the Department of Automotive Engineering (Automotive-Computer Convergence), Hanyang University, Seoul 04763, Republic of Korea (e-mail: w961227@hanyang.ac.kr; myungseop@hanyang.ac.kr).

Digital Object Identifier 10.1109/TTE.2024.3431948

altering the pole–slot combination and slot opening width. However, the effect on vibration of tangential force was not considered.

Therefore, a pole-frequency vibration reduction method that addresses both radial and tangential AEFDs, as well as the tooth modulation effect, is imperative. In this study, we propose and develop a pole-frequency vibration reduction design considering the vibration suppression effect of radial and tangential AEFDs, and the reduction of the tooth modulation effect by altering the pole–slot combination. Initially, simulations and tests were conducted to analyze a prototype of an 18-slot 16-pole (18S16P) surface-mounted PMSM. These revealed that the significant pole-frequency vibration occurs due to the vibration-enhancing effect of the lowest spatial order radial and tangential AEFDs, and the tooth modulation effect of the pole-number order radial AEFD. Subsequently, the pole–slot combination of the vibration reduction model was determined, wherein vibrations induced by the radial and tangential AEFDs suppress each other, facilitated by an analytical relationship between the spatial phases of the lowest order radial and tangential AEFDs. Furthermore, the proposed model significantly reduced pole-frequency radial vibration by increasing the lowest spatial harmonic order caused by the tooth modulation effect. Finally, the efficacy of the proposed model was validated through tests.

II. Analysis of Pole-Frequency Vibration

In this study, an 18S16P FSCW PMSM is analyzed. This pole–slot combination of PMSMs is widely used in several applications due to their high fundamental winding factor, low harmonic winding factor, low cogging torque, and good manufacturability [23], [24], [25]. Since large vibrations are caused by pole-frequency electromagnetic forces, the causes of pole-frequency vibration in the 18S16P PMSM are analyzed in this section. Specifically, the vibration enhancement effect resulting from the lowest order radial and tangential AEFDs, along with the tooth modulation effect, was investigated. Fig. 1 shows a cross-sectional view of the half model, and Table I outlines the specifications of the prototype investigated in this study. Fig. 2 shows the test results of the radial displacement measured data under both no-load and rated load conditions. As shown in Fig. 2, the most significant displacement occurred at pole frequency, which corresponds to twice the fundamental electrical frequency, $2f_e$.

A. Analysis of the Lowest Spatial Harmonic Order of Radial and Tangential AEFDs

The lowest spatial order of the AEFD in the FSCW PMSM is smaller than the pole number, which causes dominant vibrations [9]. In addition, the lowest spatial order tangential AEFD also causes large radial vibration [11]. This is because the tangential AEFDs are applied to the end of the tooth, inducing a moment in the stator yoke. Therefore, the lowest spatial order radial and tangential AEFDs were analyzed. Specifically, the spatial phases of these AEFDs were examined. According to the Maxwell stress tensor method, the radial and

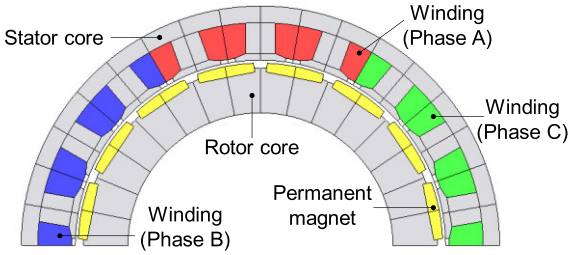

Fig. 1. Configuration of the 18S16P PMSM prototype.

TABLE I
Specifications of the 18S16P PMSM Prototype

Item	Unit	Value
Number of poles/slots	-	16/18
Stator/rotor outer diameter	mm	130.0/99.0
Stack length	mm	20.0
Tooth width	mm	8.0
Yoke width	mm	4.5
Air-gap length	mm	0.8
PM height	mm	3.0
PM width	mm	15.5
PM remanence	T	1.32
Slot opening width	mm	4.0
Number of series turns per phase	-	45
Rated speed	rpm	2000
Rated torque	Nm	5.0
Rated current	A_{rms}	28.0
Rated current density	A_{rms}/mm^2	14.7

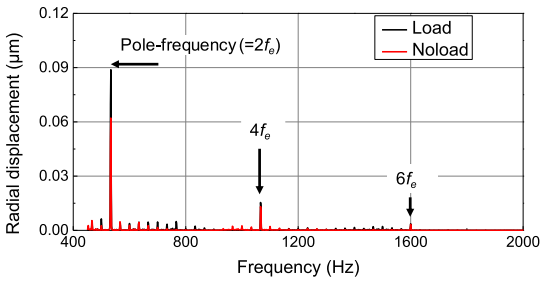

Fig. 2. Vibration test results of the 18S16P PMSM prototype.

tangential AEFDs can be expressed as

$$f_r = \frac{B_r^2 - B_t^2}{2\mu_0} \approx \frac{B_r^2}{2\mu_0} \tag{1}$$

$$f_t = \frac{B_r B_t}{\mu_0} \tag{2}$$

where f_r and f_t are the radial and tangential AEFDs, respectively; B_r and B_t are the radial and tangential air-gap magnetic flux densities, respectively; and μ_0 is the vacuum permeability. Since the tangential magnetic flux density is significantly lower than the radial magnetic flux density, it can be neglected in (1). Therefore, the slotted air-gap magnetic flux density can be expressed in terms of the slotless PM field, armature reaction, and complex relative specific permeance as follows [21]:

$$B_r \approx (B_{\mathrm{PM}} + B_{\mathrm{arm}})\lambda_a \tag{3}$$

$$B_t \approx -(B_{\mathrm{PM}} + B_{\mathrm{arm}})\lambda_b \tag{4}$$

$$B_{\mathrm{PM}} = B_m \cos(\omega t - p\theta) \tag{5}$$

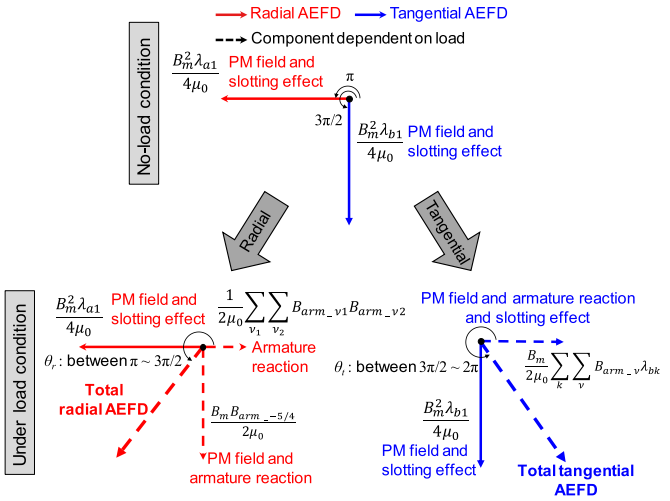

Fig. 3. Vector distribution of the lowest spatial order radial and tangential AEFDs at pole frequency.

$$B_{\text{arm}} = \sum_{\nu} B_{\text{arm\_}\nu} \cos\left(\omega t - \nu p\theta \pm \frac{\pi}{2}\right) \tag{6}$$

$$\lambda_a = 1 + \sum_{k} \lambda_{ak} \cos\left(ks\theta + \pi\right) \tag{7}$$

$$\lambda_b = \sum_{k} \lambda_{bk} \cos\left(ks\theta + \frac{\pi}{2}\right) \tag{8}$$

where B_{PM} and B_{arm} are the slotless radial magnetic flux densities caused by the PM field and armature reaction, respectively; ν is the spatial harmonic order of the armature reaction in one electrical period; B_m is the amplitude of the fundamental radial magnetic flux density caused by the PM field; $B_{\text{arm\_}\nu}$ is the amplitude of the νth spatial harmonic order of the radial magnetic flux density caused by the armature reaction; ω is the electrical angular velocity; t is the time; p is the pole pair; θ is the mechanical angle; λ_a and λ_b are the real and imaginary components of the complex relative specific permeance, respectively; λ_{ak} and λ_{bk} are the amplitudes of the real and imaginary relative specific permeance of the kth harmonic, respectively; s is the slot number; and k is an integer. The "±" sign in (6) takes "+" when $\nu > 0$ and "–" when $\nu < 0$. In this study, only the fundamental frequency of the armature reaction was considered, assuming that a sinusoidal current was applied. In addition, the harmonic components of the PM field were neglected for simplification because the fundamental component of the magnetomotive force of the PM field is the largest. By substituting (3) and (5)–(7) into (1), the lowest spatial order radial AEFD at pole frequency was derived as (9), as shown at the bottom of the page 4. Similarly, (3)–(8) were substituted into (2) to derive the lowest spatial order tangential AEFD at pole frequency as (10), as shown at the bottom of the next page. Here, $f_{r,\text{lowest}}$ and $f_{t,\text{lowest}}$ are the lowest spatial order radial and tangential AEFD at pole frequency, respectively. The square component of the slotting effect, the interaction between the square components of the armature reaction, and the slotting effect were neglected since its amplitude is relatively small.

Under a no-load condition without the armature reaction, only the interaction between the PM field and the slotting effect exists. Since the sign of the lowest spatial order of the radial and tangential AEFDs is negative ($-2 = 2p - s$) for the 18S16P PMSM, the spatial phases of the lowest order radial and tangential AEFDs at $2f_e$ are π and $3\pi/2$, respectively. If the lowest spatial harmonic order of the AEFD was positive, the spatial phase would take a negative sign in (9) and (10), resulting in $-\pi$ and $-3\pi/2$, respectively.

TABLE II
AMPLITUDE AND PHASE OF LOWEST ORDER AEFD AT $2f_e$

Item	Source	Amplitude	Phase
Radial AEFD	Interaction of PM field and slotting effect	$B_m^2\lambda_{a1}/4\mu_0$	π
	Armature reaction	$\sum_{\nu 1}\sum_{\nu 2} B_{arm\_\nu 1}B_{arm\_\nu 2}/2\mu_0$	0
	Interaction of PM field and armature reaction	$B_m B_{arm\_-5/4}/2\mu_0$	$3\pi/2$
Tangential AEFD	Interaction of PM field and slotting effect	$B_m^2\lambda_{b1}/4\mu_0$	$3\pi/2$
	Interaction of PM field and armature reaction and slotting effect	$\sum_{k}\sum_{\nu} B_m B_{arm\_\nu}\lambda_{bk}/2\mu_0$	0

Under load conditions with armature reaction, the spatial phase of the lowest order radial AEFD at $2f_e$ is determined by the amplitude of the load and slotting effect. The interaction among the PM field, armature reaction, and slotting effect [fourth component in (9)] is insignificant because they cancel each other out when the signs of ν_1 and ν_2 are different. With increasing load, the interaction between the PM field and slotting effect suppresses the armature reaction [the first and third components in (9)], where their spatial phases are π and 0, respectively. Simultaneously, the amplitude of the interaction between the PM field and armature reaction increases [second component in (9)], corresponding to a spatial phase of $3\pi/2$. Consequently, the spatial phase of the lowest order radial AEFD converges toward $3\pi/2$ with increasing load. The spatial phase of the lowest order tangential AEFD is also determined by the amplitude of the load and the slotting effect. As the load increases, the amplitude of the interaction among the PM field, armature reaction, and slotting effect [second component in (10)], where their spatial phase is 0, increases. Simultaneously, the amplitude of the interaction between the PM field and slotting effect [first component in (10)] remains constant, where their spatial phase is $3\pi/2$. Consequently, the spatial phase of the tangential AEFD converges toward 0 with increasing load. Fig. 3 and Table II show the amplitude and spatial phase relationship of the lowest radial and tangential AEFDs under no-load and load conditions. Under the no-load condition, the spatial phase of the tangential AEFD leads to that of the radial AEFD by $\pi/2$. Similarly, under the load conditions, the spatial phase of the tangential AEFD leads to that of the radial AEFD by approximately $\pi/2$ despite its dependency on the amplitude of the load and slotting effect.

To verify the spatial phase relationship between the analytically derived lowest order radial and tangential AEFDs, 2-D electromagnetic finite element analysis (FEA) was performed. Fig. 4 shows the 2-D FEA results of the amplitudes and spatial phases of the lowest order radial and tangential AEFDs at $2f_e$ according to the load conditions. As the load increased, the

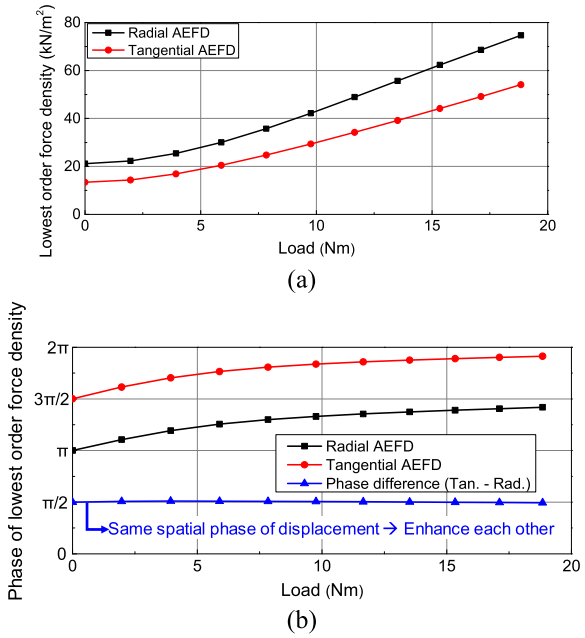

Fig. 4. Amplitude and phase of the lowest order radial and tangential AEFDs of the 18S16P PMSM at pole frequency. (a) Amplitude. (b) Phase.

amplitudes of the lowest order radial and tangential AEFDs also increased. In addition, as the load increased, the spatial phases of the lowest order radial and tangential AEFDs also increased. However, the spatial phase difference between the lowest order radial and tangential AEFDs remained almost constant at $\pi/2$, as shown in Fig. 4(b). The spatial phases of the radial and tangential AEFDs significantly affected the radial vibration of the PMSM. The radial force and radial vibration caused by the radial force occur in the same spatial phase, whereas the tangential force leads the radial vibration

TABLE III
PHASE RELATIONSHIP OF LOWEST ORDER AEFDS AND RADIAL VIBRATION OF THE 18S16P PMSM AT $2f_e$

Condition	Item	Radial force	Tangential force
No-load	Spatial phase of force	π	$3\pi/2$
	Phase of radial vibration	π	π
	Phase difference of radial vibration	0 (enhance each other)	
Load	Spatial phase of force	$\pi \sim 3\pi/2$	$3\pi/2 \sim 2\pi$
	Phase of radial vibration	$\pi \sim 3\pi/2$	$\pi \sim 3\pi/2$
	Phase difference of radial vibration	Almost 0 (enhance each other)	

caused by the tangential force by $\pi/2$. Reflecting these phase relationships, the spatial phases of the radial and tangential AEFDs and radial vibration caused by these AEFDs are summarized in Table III. Regardless of the load amplitude, the radial vibrations caused by the lowest order radial and tangential AEFDs were nearly in phase. Therefore, the radial vibration was enhanced by the two AEFDs, which increased the vibration of the 18S16P PMSM.

To analyze the effect of the spatial phase relationship of the lowest order radial and tangential AEFDs on the radial vibration of PMSM, the 3-D structural FEA was conducted. Fig. 5 shows the 3-D structural FEA results obtained by applying the lowest order radial and tangential AEFDs under no-load and rated load condition. The amplitudes of the lowest order radial and tangential AEFDs are 21.2 and 13.4 kN/m^2 at no-load conditions, respectively. Also, at rated load conditions (an average torque of 5 Nm), the amplitudes of the lowest order radial and tangential AEFDs are 27.8 and 18.4 kN/m^2, respectively. Although the lowest order tangential AEFD is smaller than the radial AEFD, Fig. 5 shows that its effect on

$$f_{r,\text{lowest}} \approx \underbrace{\frac{B_m^2 \lambda_{a1}}{4\mu_0}\cos\{2\omega t-(2p-s)\theta+\pi\}}_{\text{PM field \& slotting effect}} + \underbrace{\frac{B_m B_{\text{arm}\_\nu}}{2\mu_0}\cos\left\{2\omega t-(1+\nu)p\theta+\frac{3\pi}{2}\right\}}_{\text{PM field \& armature reaction } (\nu<0)}$$
$$+ \underbrace{\frac{1}{2\mu_0}\sum_{\nu_1}\sum_{\nu_2} B_{\text{arm}\_\nu 1} B_{\text{arm}\_\nu 2}\cos\{2\omega t-(\nu_1+\nu_2)p\theta\}}_{\text{Armature reaction}(\nu_1\times\nu_2<0)}$$
$$+ \underbrace{\frac{B_m}{2\mu_0}\sum_{k}\sum_{\nu}\left[\underbrace{B_{\text{arm}\_\nu}\lambda_{ak}\cos\left\{2\omega t-(p+\nu p-ks)\theta+\frac{3\pi}{2}\right\}}_{\nu<0} + \underbrace{B_{\text{arm}\_\nu}\lambda_{ak}\cos\left\{2\omega t-(p+\nu p+ks)\theta+\frac{\pi}{2}\right\}}_{\nu<0}\right]}_{\text{PM field \& armature reaction \& slotting effect}} \quad (9)$$

$$f_{t,\text{lowest}} \approx \underbrace{\frac{B_m^2 \lambda_{b1}}{4\mu_0}\cos\left\{2\omega t-(2p-s)\theta+\frac{3\pi}{2}\right\}}_{\text{PM field \& slotting effect}}$$
$$+ \underbrace{\frac{B_m}{2\mu_0}\sum_{k}\sum_{\nu}\left[\underbrace{B_{\text{arm}\_\nu}\lambda_{bk}\cos\{2\omega t-(p+\nu p-ks)\theta\}}_{\nu>0} + \underbrace{B_{\text{arm}\_\nu}\lambda_{bk}\cos\{2\omega t-(p+\nu p+ks)\theta\}}_{\nu<0}\right]}_{\text{PM field \& armature reaction \& slotting effect}} \quad (10)$$

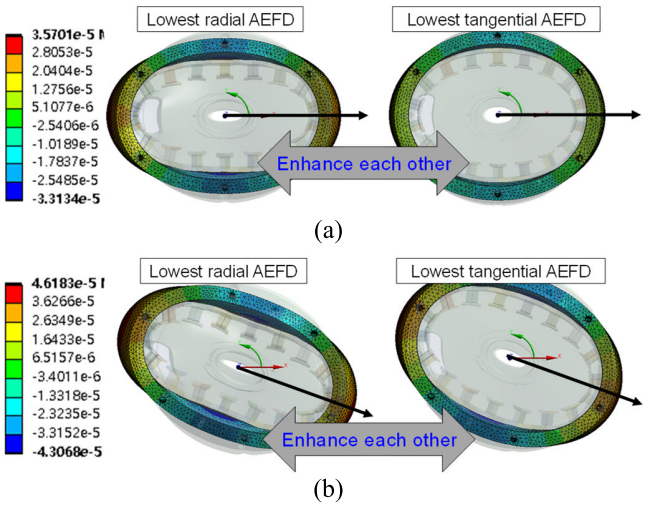

Fig. 5. 3-D structural FEA results of the 18S16P PMSM obtained by applying the lowest order (−2nd) AEFD at pole frequency. (a) No-load condition. (b) Rated load condition. (Unit: mm and scale: 6×10^5.)

vibration is not negligible. Consistent to previous analyses, it was confirmed that the radial vibration caused by the lowest order radial and tangential AEFDs mutually enhanced each other, regardless of load conditions. Given that the radial vibration caused by the lowest order tangential AEFD was comparable in amplitude to that caused by the radial AEFD, this radial vibration-enhancing effect significantly deteriorated the pole-frequency radial vibration characteristics of PMSM. Furthermore, the amplitudes of the lowest order radial and tangential AEFDs increased proportionally with the load. Consequently, the pole-frequency radial vibration characteristics of the PMSM degraded as the load increased.

B. Electromagnetic Tooth Modulation Effect

In several existing studies, higher spatial order radial AEFDs have been neglected. However, high spatial order radial AEFDs can be modulated into low spatial order radial forces, as shown in Fig. 6, causing significant vibration [12]. If the spatial order of the original AEFD is greater than half of the slot number, abs(r) > s/2, then the AEFD is modulated into a low spatial order as

$$f^r = f^{r\prime} \cos\left[(|r| - ks)\theta + \omega^r t + \beta^r\right] \tag{11}$$

where superscript r denotes the spatial order of the AEFD, k is an integer, and $f^{r\prime}$ denotes the modulated force density. A large pole-number (16th = 2pth) spatial order radial AEFD inevitably occurred due to the synthesis of the fundamental component of the PM field and armature reaction, and it is modulated into a 2nd-order concentrated radial force.

The amplitude and spatial phase of the modulated force are determined based on the amplitude and phase of the original AEFD and its spatial harmonic order. The modulated radial force can be calculated from the radial and tangential AEFDs as follows:

$$F_{r,z} = R_{\mathrm{si}} L_{\mathrm{stk}} \int_{\theta_z - \pi/s(1-\alpha)}^{\theta_z + \pi/s(1-\alpha)} \{f_r \cos(\theta_z - \theta) + f_t \sin(\theta_z - \theta)\} d\theta \tag{12}$$

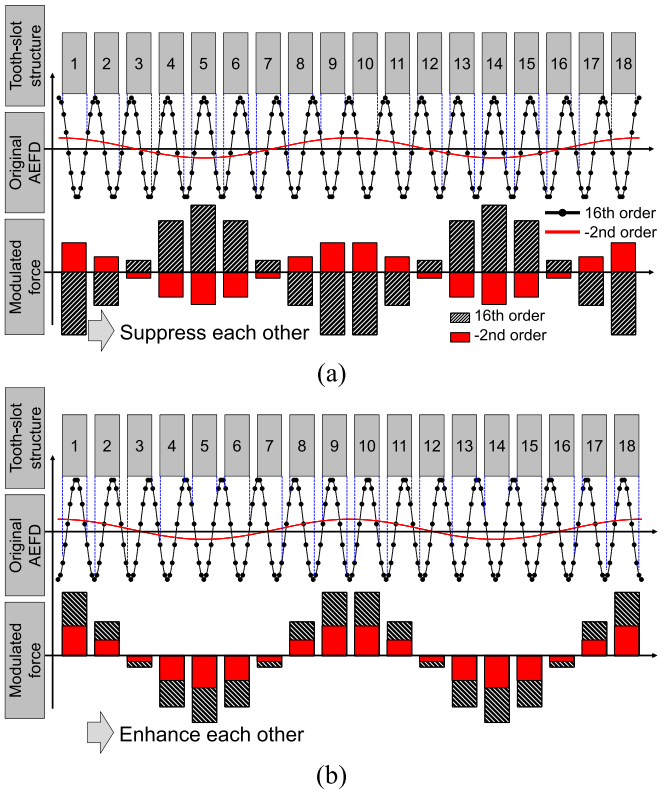

Fig. 6. Tooth modulation effect of the 16th-order radial AEFD by 18 tooth-slot structure. (a) Same phase. (b) Opposite phase.

where $F_{r,z}$ is the modulated radial force at the zth tooth; f_r and f_t are the radial and tangential AEFDs, respectively; R_{si} is the inner radius of the stator; L_{stk} is the stack length; θ is the mechanical angle; θ_z is the mechanical angle of the zth tooth center; α is the slot opening pitch; and z is the tooth number. The slot opening pitch indicates the ratio of the slot opening angle to the slot angle, and it can lie between 0 and 1. For instance, if the slot opening pitch is 8° for 18 slots, the slot opening pitch is 0.4. Considering that the pole-number order tangential AEFD is relatively small compared to that of radial AEFD, the tangential AEFD in (12) can be neglected. The modulated radial force caused by the nth spatial order radial AEFD with 0 spatial phase is expressed as follows:

$$\begin{aligned} F_{r,z} &= f_{r,n} R_{\mathrm{si}} L_{\mathrm{stk}} \int_{\theta_z - \pi/s\beta}^{\theta_z + \pi/s\beta} \{\cos(n\theta)\cos(\theta_z - \theta)\} d\theta = f_{r,n} R_{\mathrm{si}} L_{\mathrm{stk}} \\ &\times \frac{2\cos(n\theta_z)\left\{n\cos\left(\frac{\pi\beta}{s}\right)\sin\left(\frac{n\pi\beta}{s}\right) - \sin\left(\frac{\pi\beta}{s}\right)\cos\left(\frac{n\pi\beta}{s}\right)\right\}}{n^2 - 1} \end{aligned} \tag{13}$$

where $f_{r,n}$ is the amplitude of the nth spatial order radial AEFD and 1 – α is expressed as β to simplify the equation. Since the pole-number order radial AEFD has the largest amplitude, other harmonics were neglected [22]. Therefore, it is necessary to analytically analyze the amplitude and phase of the pole-number order radial AEFD since it has the largest amplitude. By substituting (3) and (5)–(7) into (1), the pole-number order radial AEFD at pole frequency can be derived as (14), as shown at the bottom of the page 7. Here, f_{r_pole} is the pole-number order radial AEFD at pole frequency.

TABLE IV
SPATIAL PHASE OF THE LOWEST, POLE-NUMBER ORDER, AND MODULATED RADIAL FORCE

Item	Spatial phase at no-load	Spatial phase at load
Lowest order radial AEFD	π	π ~$3\pi/2$
Pole-number order radial AEFD	0	0~ $\pi/2$
Modulated radial force	π	π~$3\pi/2$

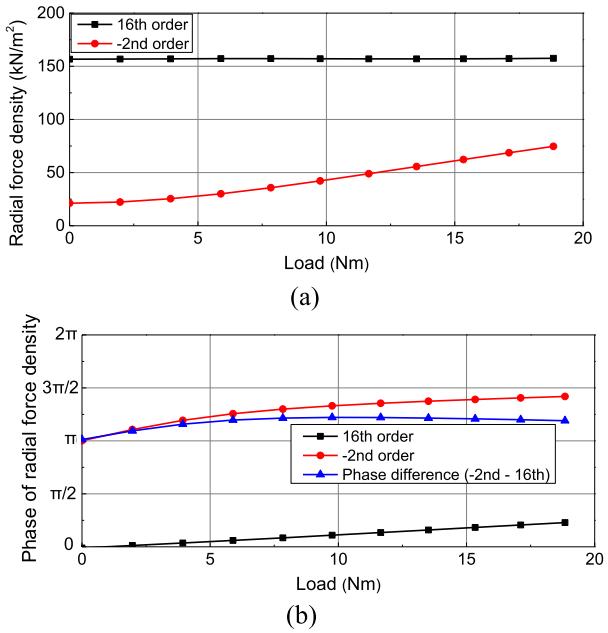

Fig. 7. Pole-number order and lowest order radial AEFD of the 18S16P PMSM at pole frequency. (a) Amplitude. (b) Phase.

The square component of the slotting effect and the interaction between the square components of the armature reaction and slotting effect were neglected.

Under the no-load condition, the pole-number order radial AEFD is caused by the PM field only, and its spatial phase is 0. Under the load condition, the effect of the interaction among the PM field, armature reaction, and slotting effect [fifth component in (14)] is negligible since they cancel each other out when the sign of ν is opposite. The interaction between the PM field and armature reaction [second component in (14)] increases as the load increases, where their spatial phase is $\pi/2$. Consequently, the spatial phase of the pole-number order radial AEFD under load conditions is determined to be between 0 and $\pi/2$.

Since the center of a slot opening is located at the point where the mechanical angle is 0, θ_z can be expressed as $\pi/s + 2\pi(z–1)/s$, and for 18S16P PMSM, $2p$ equals $s– 2$. Then, (13) can be expressed as follows:

$$F_{r,z} = f_{r,2p} R_{\mathrm{si}} L_{\mathrm{stk}} K_r(\alpha) \cos\left\{\pi - \frac{(2z-1)2\pi}{s}\right\} \tag{15}$$

where

$$K_r(\alpha) = \frac{2\left\{n\cos\left(\frac{\pi\beta}{s}\right)\sin\left(\frac{n\pi\beta}{s}\right) - \sin\left(\frac{\pi\beta}{s}\right)\cos\left(\frac{n\pi\beta}{s}\right)\right\}}{n^2-1}. \tag{16}$$

Therefore, the spatial phase of the modulated radial force is at the position where the mechanical angle 0 is π. The spatial phase of the lowest order radial AEFD, pole-number order radial AEFD, and modulated radial force are summarized in Table IV. As shown in Table IV, the spatial phase of the lowest order radial AEFD and the modulated radial force caused by the pole-number order radial AEFD are the same. Therefore, the radial vibration caused by the lowest order radial AEFD and the modulated radial force enhance each other.

To verify the spatial phase relationship between the analytically analyzed lowest order radial AEFD and pole-number order radial AEFD, 2-D electromagnetic FEA was conducted. Fig. 7 shows the 2-D electromagnetic FEA results of the amplitude and phase of the radial AEFD based on the load conditions. As the load increases, the amplitude of the lowest order radial AEFD increases, while the amplitude of the pole-number order radial AEFD remains almost constant. Thus, the tooth modulation effect has a significant impact mainly under no-load and low-load conditions. Furthermore, the spatial phase difference between the pole-number order and lowest order radial AEFD was almost π, as shown in Fig. 7(b). The 16th-order radial AEFD was modulated into a –2nd-order concentrated force by the 18 tooth-slot structure with its phase shifted by π, as shown in Fig. 6(a) and Table IV. Therefore, the original lowest order (–2nd) radial AEFD and –2nd-order modulated force caused by the pole-number order radial AEFD were in phase, as shown in Fig. 6(b). This enhanced the pole-frequency radial vibration of the 18S16P PMSM.

To verify the radial vibration enhancement effect of the lowest order radial AEFD and the modulated radial force caused by the pole-number order radial AEFD as analyzed in Table IV, 3-D structural FEA was conducted. Fig. 8 shows the 3-D structural FEA results of the 18S16P PMSM obtained by applying the pole-number order radial AEFD under no-load and rated load conditions. Due to the tooth modulation effect, the radial vibration caused by the pole-number order radial AEFD was larger than that caused by the lowest order radial AEFD, as shown in Fig. 5. The radial displacement caused by the total forces under no-load and rated load conditions is shown in Fig. 9. It was confirmed that the phase of the radial displacement was nearly identical to that caused by the lowest order radial, tangential, and pole-number order radial AEFDs. The amplitudes of the radial displacements caused by the lowest order radial, tangential, and pole-number order radial AEFDs are summarized in Table V. It was confirmed that the radial vibration at the pole frequency of the 18S16P PMSM was exacerbated by these three types of forces.

In Section III, a radial vibration reduction design at $2f_e$ considering the causes of significant vibrations are conducted.

III. VIBRATION REDUCTION BY MODIFYING POLE NUMBER

Although modifying only the configuration of the PMSM could potentially reduce the radial vibration at pole frequency, the resulting reduction in vibration may be insignificant. The radial vibration enhancement effect caused by the lowest order radial and tangential AEFDs, as well as the 2nd-order modulated force due to the tooth modulation effect, cannot

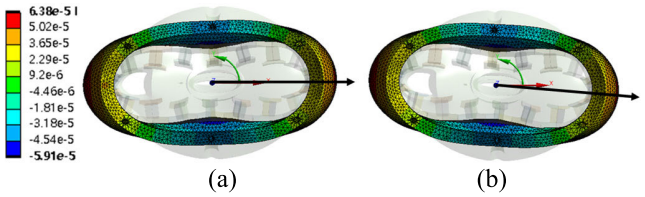

Fig. 8. 3-D structural FEA results of the 18S16P PMSM obtained by applying the pole-number order (16th) radial AEFD at pole frequency. (a) No-load condition. (b) Rated load condition. (Unit: mm and scale: 6×10^5.)

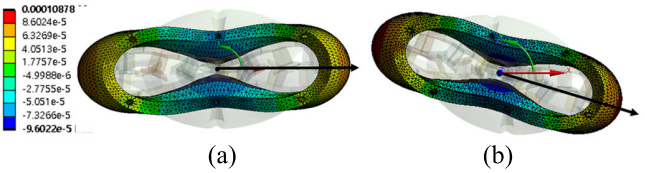

Fig. 9. 3-D structural FEA results of the 18S16P PMSM obtained by applying all forces at pole frequency. (a) No-load condition. (b) Rated load condition. (Unit: mm and scale: 6×10^5.)

be eliminated. Therefore, to mitigate the radial vibration enhancement effect, the following two conditions are required.

1) The spatial phase difference in the radial vibration caused by the lowest order radial and tangential AEFDs should be π. To satisfy this condition, the lowest spatial order of the AEFD should have a "+" sign.
2) The spatial order of the radial modulated force generated by the tooth modulation effect should differ from the original lowest spatial order of the radial AEFD. To satisfy this condition, the pole–slot combination should follow the relationship $\mathrm{GCD}(s, 2p) < |2p - s|$, where GCD denotes the greatest common divisor.

Similar to the discussion in the previous section, when the sign of the lowest order is positive, the spatial phases in (9) and (10) become negative, indicating that the vector distribution shown in Fig. 3 undergoes symmetric transposition on the x-axis. Fig. 10 shows the vector distribution of the lowest spatial order radial and tangential AEFDs when the sign of the lowest order is "+." The spatial phase of the lowest order radial AEFD leads to the lowest order tangential AEFD by approximately $\pi/2$. Thus, the phase difference between the radial displacements caused by the two forces

TABLE V
AMPLITUDE OF RADIAL DISPLACEMENT BY SOURCE AT $2f_e$

Force	Radial displacement (μm)	
	No-load	Rated load
Lowest order radial AEFD	0.0357	0.0462
Lowest order tangential AEFD	0.0201	0.0276
Pole-number order radial AEFD	0.0638	0.0641
Sum (applying all forces)	0.0932	0.1088

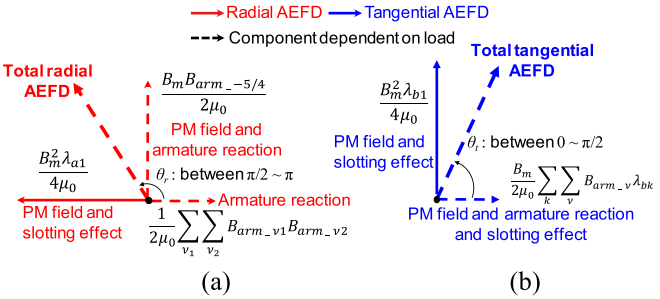

Fig. 10. Vector distribution of the lowest spatial order radial and tangential AEFDs at pole frequency when the sign of the lowest spatial order is "+." (a) Radial AEFD. (b) Tangential AEFD.

is approximately π. The radial vibrations caused by these two forces cancel each other, resulting in a reduction in vibration.

To satisfy conditions 1 and 2 at $2f_e$, the pole–slot combination of the PMSM should be adjusted. The lowest force orders and absolute values of the difference between the number of poles and slots, expressed as $|2p - s|$, and fundamental winding factor according to the pole–slot combination of the FSCW PMSM are listed in Table VI. In this study, pole–slot combinations with $q > 0.5$ and $q < 0.25$, where q denotes the number of slots per pole per phase, were excluded. For $q > 0.5$, the fundamental winding factor is reduced with concentrated winding, while for $q < 0.25$, multiple north and south poles interact with a single stator tooth, leading to inefficiency. Among the pole–slot combinations listed in Table VI, both the 18S14P and 21S16P PMSMs satisfy conditions 1 and 2. However, because the lowest force order of the 21S16P PMSM is 1, it is expected to exhibit inferior vibration characteristics owing to the unbalanced force. A pole–slot combination with a pole-to-slot number ratio of 4:3 and a

$$
\begin{aligned}
f_{r\_\mathrm{pole}} \approx\ & \underbrace{\frac{B_m^2}{4\mu_0}\cos(2\omega t - 2p\theta)}_{\text{PM field}} + \underbrace{\frac{B_m B_{\mathrm{arm}\_\nu}}{2\mu_0}\cos\left(2\omega t - 2p\theta + \frac{\pi}{2}\right)}_{\text{PM field \& armature reaction } (\nu=1)} + \underbrace{\frac{B_{\mathrm{arm}\_\nu}^2}{4\mu_0}\cos(2\omega t - 2p\theta + \pi)}_{\text{Armature reaction } (\nu=1)} \\
& + \underbrace{\sum_{\nu_1}\sum_{\nu_2}\frac{B_{\mathrm{arm}\_\nu 1} B_{\mathrm{arm}\_\nu 2}}{2\mu_0}\cos\{2\omega t - (\nu_1 + \nu_2)p\theta\}}_{\text{Armature reaction } (\nu_1 \times \nu_2 < 0)} \\
& + \underbrace{\frac{B_m}{2\mu_0}\sum_k\sum_\nu\left[\underbrace{B_{\mathrm{arm}\_\nu}\lambda_{ak}\cos\left\{2\omega t - (p + \nu p - ks)\theta + \frac{3\pi}{2}\right\}}_{\nu>0} + \underbrace{B_{\mathrm{arm}\_\nu}\lambda_{ak}\cos\left\{2\omega t - (p + \nu p + ks)\theta + \frac{\pi}{2}\right\}}_{\nu<0}\right]}_{\text{PM field \& armature reaction \& slotting effect}} \qquad (14)
\end{aligned}
$$

TABLE VI
VIBRATION CHARACTERISTICS AND WINDING FACTOR BASED ON THE POLE–SLOT COMBINATION

Slot number	Pole number (lowest force order, $\lvert 2p-s \rvert$, fundamental winding factor)								
	2	4	6	8	10	12	14	16	20
3	–1 / 1 / 0.866	+1 / 1 / 0.866	q<1/4						
6	q>1/2	–2 / 2 / 0.866	-	+2 / 2 / 0.866	q<1/4				
9		q>1/2	–3 / 3 / 0.866	–1 / 1 / 0.945	+1 / 1 / 0.945	+3 / 3 / 0.866	q<1/4		
12			q>1/2	–4 / 4 / 0.866	–2 / 2 / 0.933	-	+2 / 2 / 0.933	+4 / 4 / 0.866	q<1/4
15				q>1/2	–5 / 5 / 0.866	-	–1 / 1 / 0.951	+1 / 1 / 0.951	+5 / 5 / 0.866
18					q>1/2	–6 / 6 / 0.866	**+2 / 4 / 0.902**	–2 / 2 / 0.945	+2 / 2 / 0.945
21						q>1/2	–7 / 7 / 0.866	+1 / 5 / 0.890	–1 / 1 / 0.953
24							q>1/2	–8 / 8 / 0.866	–4 / 4 / 0.933
27								q>1/2	–1 / 7 / 0.877
30									–10 / 10 / 0.866
36									q>1/2

large pole number, such as 15S20P PMSM, is considered to be a good option for a small radial vibration because the sign of the lowest order is "+." However, because the pole–slot combination with a pole-to-slot number ratio of 4:3 has a low fundamental winding factor of 0.866 and relatively large 5th and 7th harmonic winding factors of 0.866, the combination was considered disadvantageous in terms of output torque and torque ripple. Therefore, the 18P14S PMSM is considered as a good alternative with good pole-frequency radial vibration characteristics and a high winding factor. The selection criteria for the 18S14P PMSM as an improved model are summarized as follows.

1) The sign of the lowest force order is "+," which leads to the suppression effect of the radial vibration caused by the lowest order radial and tangential AEFDs at $2f_e$.

2) The difference between the pole and slot numbers differs from the lowest force order, which leads to a small tooth modulation effect.

3) The fundamental winding factor is high, which leads to high efficiency and torque density.

Thus, an 18S14P PMSM was designed to satisfy the output torque of the 18S16P PMSM, and a vibration analysis was performed to confirm the vibration reduction effect. As the fundamental winding factor was reduced from 0.945 to 0.902, the number of turns per tooth was increased by one to maintain the back electromotive force (BEMF). As the number of turns increased, the tooth and yoke widths decreased to satisfy the same current density and slot fill factor.

Although optimizing the 18S14P PMSM could potentially reduce radial vibration, this study focused exclusively on validating the reduction of pole-frequency radial vibration by varying the number of poles. Consequently, only the number poles were modified, while the other geometric variables remained unchanged. The specifications that changed from the 18S16P PMSM to the 18S14P PMSM are summarized in Table VII.

The BEMF at no-load condition and torque waveforms at rated load conditions were calculated using 2-D electromagnetic FEA, and the results are shown in Fig. 11. The BEMFs and output torques of both PMSMs were nearly identical as intended. Fig. 12 shows the 2-D FEA results of the amplitudes and spatial phases of the lowest order radial and tangential AEFDs at $2f_e$, considering various load conditions.

TABLE VII
SPECIFICATIONS OF THE 18S16P AND 18S14P PMSMS

Item	Unit	18S16P	18S14P
Number of poles/slots	-	16/18	14/18
Tooth width	mm	8.0	7.65
Yoke width	mm	4.5	4.3
PM width	mm	15.5	17.7
Number of series turns per phase	-	45	48

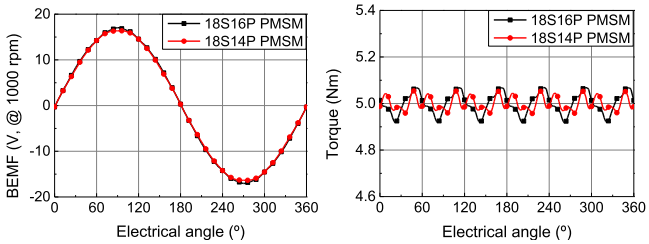

Fig. 11. BEMF and rated torque waveforms of the 18S16P and 18S14P PMSMs. (a) BEMF at 1000 rpm. (b) Rated torque.

It can be seen that the amplitudes of the lowest radial and tangential AEFDs of the 18S14P PMSM are considerably smaller than those of the 18S16P PMSM. This phenomenon can be explained as follows. The lowest order AEFD of the 18S16P PMSM is primarily generated by the interaction between the PM field and slotting effect, as well as by the interaction between the fundamental component of the armature reaction and slotting effect. Due to the relatively large amplitudes of the PM field and the fundamental armature reaction component, the lowest order AEFD of the 18S16P PMSM is correspondingly large. In contrast, in the 18S14P PMSM, the lowest order AEFD is not generated by neither the PM field and slotting effect or the interaction of the fundamental component of the armature reaction and slotting effect. Instead, inclusion of the subharmonic component of the armature reaction (e.g., $\nu_1 = -5/7$, $\nu_2 = 1$) is necessary to generate the lowest order AEFD [9], [23]. Generally, the amplitudes of the subharmonic components in the armature reaction are relatively small. Consequently, the amplitude of the lowest order AEFD of the 18S14P PMSM is also relatively small.

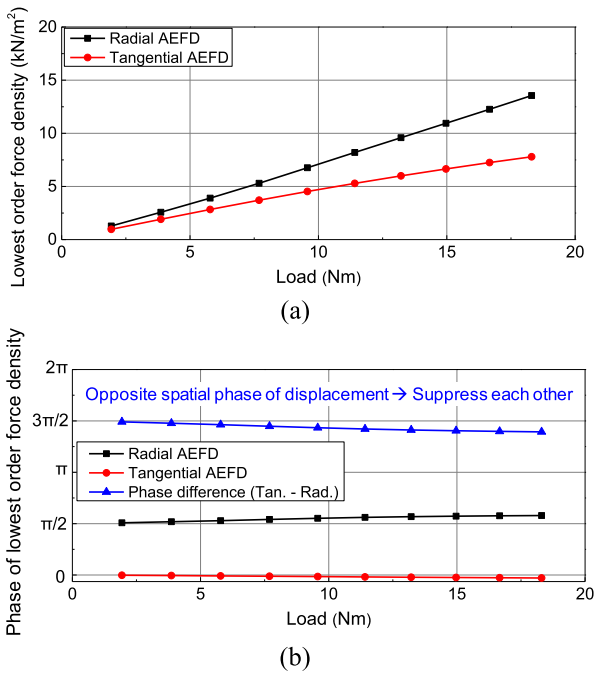

Fig. 12. Amplitude and phase of the lowest order radial and tangential AEFDs of the 18S14P PMSM at pole frequency. (a) Amplitude. (b) Phase.

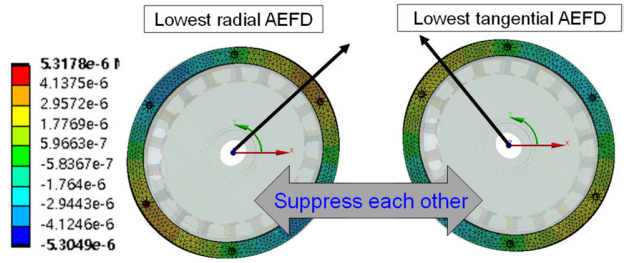

Fig. 13. 3-D structural FEA results of the 18S14P PMSM obtained by applying the lowest order (2nd) AEFD at rated load condition at pole frequency. (Unit: mm and scale: 6×10^5.)

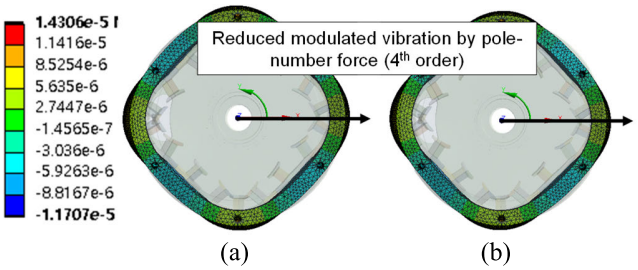

Fig. 14. 3-D structural FEA results of the 18S14P PMSM obtained by applying the pole-number order (14th) radial AEFD at rated load condition at pole frequency. (a) No-load condition. (b) Rated load condition. (Unit: mm and scale: 6×10^5.)

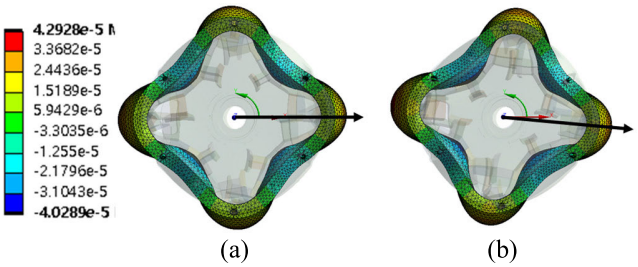

Fig. 15. 3-D structural FEA results of the 18S14P PMSM obtained by applying all forces at pole-frequency. (a) No-load condition. (b) Rated load condition. (Unit: mm and scale: 6×10^5.)

As the load increases, the amplitudes of the lowest order radial and tangential AEFDs also increased. However, the difference in their spatial phases remains nearly constant $3\pi/2$, as shown in Fig. 12(b). This indicates that the pole-frequency radial vibrations caused by the lowest order radial and tangential AEFDs have opposite phases. Therefore, the radial vibration is suppressed by the two AEFDs, resulting in a reduction of pole-frequency radial vibration in the 18S14P PMSM.

Subsequently, a 3-D structural FEA was conducted by applying the lowest order radial and tangential AEFDs along with the pole-number order radial AEFD. Fig. 13 shows the vibration analysis results at the pole frequency of the 18S14P PMSM obtained by applying the lowest order radial and tangential AEFDs. As the 2nd-order AEFD does not occur at no-load condition of the 18S14P PMSM, only results under rated load condition are shown. Consistent with previous discussions, the phase difference between the radial displacements caused by the lowest order radial and tangential AEFDs is approximately π. Therefore, the radial vibrations caused by the two forces cancel each other, resulting in small radial vibration. In addition, the lowest order (2nd) AEFD in the 18S14P PMSM was not generated by the interaction between the PM field and slotting effect but solely by the interaction between the PM field and armature reaction. As a result, the amplitude of the radial displacement was significantly reduced compared to that in the 18S16P PMSM. Fig. 14 shows the pole-frequency radial displacement of the 18S14P PMSM caused by the pole-number order radial AEFD. As the difference between the number of poles and slots of 18S14P PMSM is 4, the mode of radial displacement is also 4. As the 4th mode occurred due to the tooth modulation effect, the radial displacement of 18S14P PMSM is smaller than 2nd mode radial displacement caused by tooth modulation effect of the 18S16P PMSM. Finally, Fig. 15 shows the pole-frequency radial displacements obtained by applying all forces to the 18S14P PMSM. It can be confirmed that the 18S14P PMSM exhibits significantly smaller pole-frequency radial displacement compared to the 18S16P PMSM regardless of load conditions. This reduction in pole-frequency radial vibration is attributed to the suppression effect of the radial vibration caused by the lowest order radial and tangential AEFDs, as well as a reduced tooth modulation effect. Fig. 16 shows the pole-frequency radial displacements of the 18S16P and 18S14P PMSMs under both no-load and rated load conditions. The radial displacement was reduced by 58.9% and 60.5% under no-load and rated load conditions, respectively, by altering the pole number.

IV. Experimental Verifications

To validate the analysis and simulation results, vibration tests were conducted. Fig. 17 shows the prototypes of the 18S16P and 18S14P PMSMs. Both prototypes were fabricated with identical housing configuration to ensure a fair

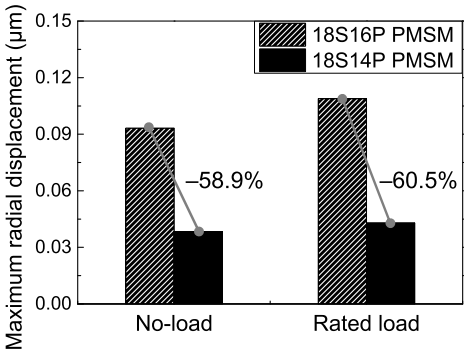

Fig. 16. Maximum radial displacement of the 18S16P and 18S14P PMSMs at $2f_e$.

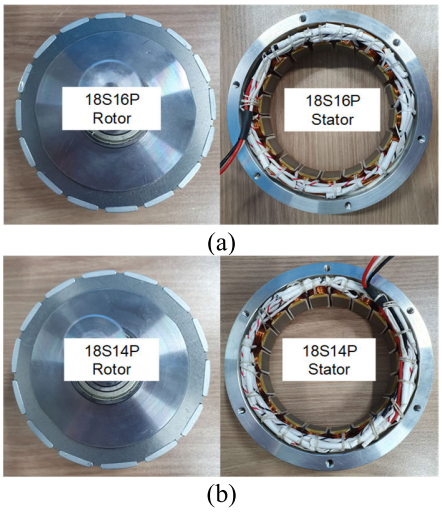

Fig. 17. Configuration of the prototypes. (a) 18S16P PMSM. (b) 18S14P PMSM.

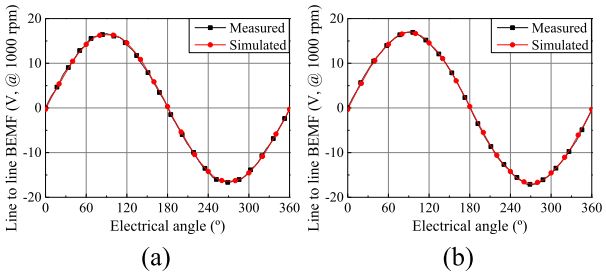

Fig. 18. No-load BEMF test and simulation results at 1000 rpm. (a) 18S16P PMSM. (b) 18S14P PMSM.

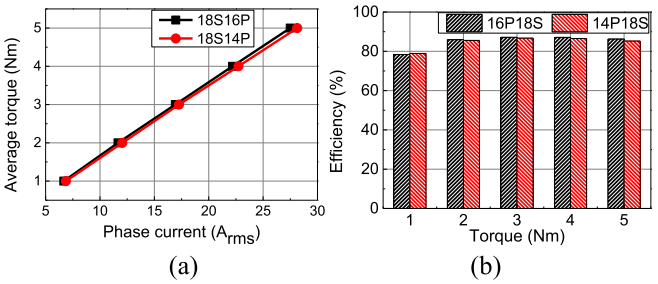

Fig. 19. Measured current–torque curve and efficiency at 2000 rpm. (a) Current–torque curve. (b) Efficiency.

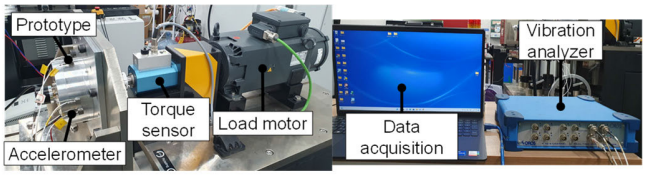

Fig. 20. Vibration test setup.

comparison, and detailed stator and rotor specifications are summarized in Table VII. To confirm whether the prototype is fabricated correctly as intended, the no-load BEMF and current–torque curve were measured. The no-load BEMF was measured by rotating the servo motor at 1000 rpm, while the current–torque curve was measured by rotating the servomotor at 2000 rpm and increasing the input current of the prototype. The measured and simulated BEMFs are shown in Fig. 18, where the error was observed to be small. Fig. 19(a) shows the current–torque curve of the prototypes, confirming similar currents for both 18S16P and 18S14P PMSMs at equivalent output torques. However, due to the larger fundamental winding factor of 0.945 for the 18S16P PMSM compared to 0.902 for the 18S14P PMSM, less current is required for the 18S16P PMSM to achieve the same output torque. Fig. 19(b) shows the measured efficiencies of the two PMSMs. With lower current required at equivalent torque levels, the 18S16P PMSM exhibits higher efficiency at higher torque due to reduced copper loss. Conversely, the 18S14P PMSM demonstrates higher efficiency at lower toque levels owing to lower iron loss.

Fig. 20 shows the vibration test setup, comprising a prototype, a torque sensor, a load motor, a vibration data acquisition tool, a vibration analyzer, and accelerometers. Four accelerometers were attached to housing surfaces. The vibration tests were conducted under no-load (0 Nm/2000 rpm), half-rated load (2.5 Nm/2000 rpm), and rated load (5.0 Nm/2000 rpm) conditions. In this study, the load motor, which is an induction motor, was controlled at a constant speed of 2000 rpm and the prototype was controlled to generate 2.5- and 5.0-Nm torque at the half-rated load and rated load conditions, respectively.

Fig. 21 shows the radial accelerations of the 18S16P and 18S14P PMSMs in time domain. However, since the primary objective of this study is to examine the reduction effect of the pole-frequency radial vibration, it is challenging to discern this effect solely through time-domain results. Therefore, to facilitate the analysis of pole-frequency radial vibration, frequency-domain radial displacements were calculated, as shown in Fig. 22. As the fundamental frequencies of the 18S14P and 18S16P PMSMs at 2000 rpm are 233.3 and 266.7 Hz, the pole frequency $2f_e$ is 466.6 and 533.3 Hz, respectively. As shown in Fig. 22, the pole-frequency radial displacement of the 18S16P PMSM was greater than that of the 18S14P PMSM regardless of the load conditions. Under the no-load condition, the pole-frequency radial displacements for the 18S14P and 18S16P PMSMs were 0.0343 and 0.0621 μm, respectively. Under the half-rated load condition, the pole-frequency radial displacements were 0.0444 μm for the 18S14P PMSM and 0.0693 μm for the 18S16P PMSM. Under the rated load condition, the pole-frequency radial displacements were 0.0558 μm for the 18S14P PMSM

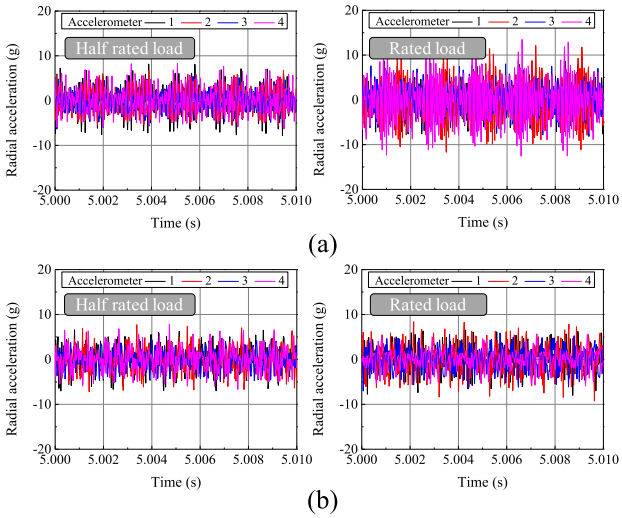

Fig. 21. Measured radial accelerations of the PMSM prototypes. (a) 18S16P PMSM. (b) 18S14P PMSM.

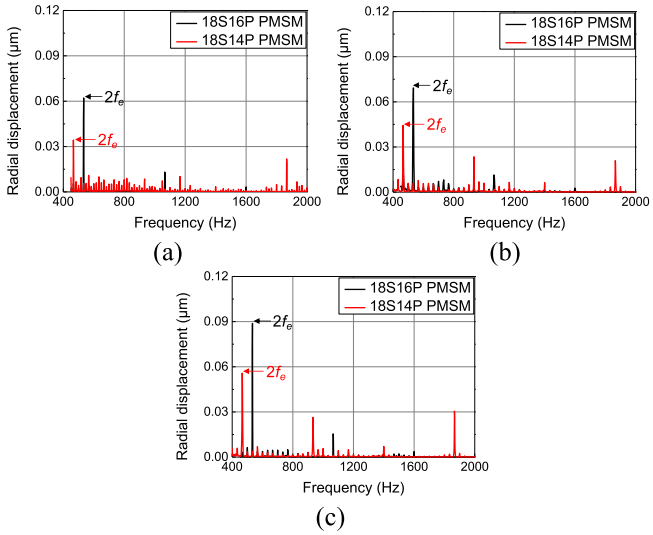

Fig. 22. Measured radial displacements of the PMSM prototypes. (a) No-load condition (@0 Nm and 2000 rpm). (b) Half rated load condition (@2.5 Nm and 2000 rpm). (c) Rated load condition (@5 Nm and 2000 rpm).

and 0.0888 μm for the 18S16 PMSM. Consequently, the pole-frequency radial displacement of the proposed 18S14P PMSM was reduced by 44.8%, 35.9%, and 37.2% under no-load, half-rated load, and rated load conditions, respectively. Although there may be some discrepancies in the numerical values between the simulation and test results, it was still confirmed that the pole-frequency radial vibration of the 18S14P PMSM is smaller than that of the 18S16P PMSM, demonstrating consistency between the simulation and test results. The error between simulation and test may occur because the structural model does not properly describe the core lamination of the stator and is difficult to reflect the exact effect of the winding. Regarding the vibration test results, it is important to note that with the exception of the pole frequency, which was a target frequency to reduce vibration, the vibration of 18S14P PMSM is larger than that of 18S16P PMSM at frequencies, such as $4f_e$ and $8f_e$. This is because the 18S16P PMSM is an optimized model, whereas the 18S14P PMSM was designed to closely resemble the configuration of the 18S16P PMSM solely to demonstrate the pole-frequency radial vibration reduction effect. If 18S14P PMSM was also optimized under the same conditions as the 18S16P PMSM, harmonic vibrations of 18S14P PMSM are expected to be reduced.

V. Conclusion

In this study, the causes of the significant pole-frequency electromagnetic radial vibration in an 18S16P PMSM were analyzed, and a pole-frequency radial vibration reduction model was proposed by altering the pole number. First, the spatial phases of the lowest spatial harmonic order radial and tangential AEFDs were analytically investigated using complex permeance. The results show that the pole-frequency radial vibrations caused by the lowest order radial and tangential AEFDs enhanced each other because the sign of the lowest force order was negative. Second, it was determined that a significant pole-frequency radial vibration was caused by the tooth modulation effect, and this vibration was enhanced by the lowest order radial and tangential AEFDs. Subsequently, based on the analysis results, the vibration reduction model (18S14P PMSM) was proposed that the pole-frequency radial vibration was suppressed by the lowest order radial and tangential AEFDs and also had small tooth modulation effect. Finally, vibration tests were conducted on the prototypes of 18S16P and 18S14P PMSMs, and the test results validated the simulated results and vibration reduction design. The research results of this article will be used to help determine appropriate pole–slot combination at an early stage when designing PMSM for applications such as robots that require small pole-frequency radial displacement.

References

[1] Z. Q. Zhu, Z. P. Xia, L. J. Wu, and G. W. Jewell, "Analytical modeling and finite-element computation of radial vibration force in fractional-slot permanent-magnet brushless machines," *IEEE Trans. Ind. Appl.*, vol. 46, no. 5, pp. 1908–1918, Jul. 2010.

[2] Z. Q. Zhu, Z. P. Xia, L. J. Wu, and G. W. Jewell, "Influence of slot and pole number combination on radial force and vibration modes in fractional slot PM brushless machines having single-and double-layer windings," in *Proc. IEEE Energy Convers. Cong. Expo.*, Sep. 2009, pp. 3443–3450.

[3] F. Lin, S. Zuo, and X. Wu, "Electromagnetic vibration and noise analysis of permanent magnet synchronous motor with different slot-pole combinations," *IET Electr. Power Appl.*, vol. 10, no. 9, pp. 900–908, 2016.

[4] W. Deng and S. Zuo, "Electromagnetic vibration and noise of the permanent-magnet synchronous motors for electric vehicles: An overview," *IEEE Trans. Transport. Electrific.*, vol. 5, no. 1, pp. 59–70, Mar. 2019.

[5] C. Ramos-Romero, N. Green, S. Roberts, C. Clark, and A. J. Torija, "Requirements for drone operations to minimise community noise impact," *Int. J. Environ. Res. Public Health*, vol. 19, no. 15, p. 9299, Jul. 2022.

[6] E. Atasoy, B. Çetin, and Ö. Bayer, "Experiment-based optimization of an energy-efficient heat pump integrated water heater for household appliances," *Energy*, vol. 245, Apr. 2022, Art. no. 123308.

[7] J. Zhou, M. Cheng, H. Wen, X. Yan, M. Tong, and W. Wang, "Modeling and suppression of torque ripple in PMSM based on the general airgap field modulation theory," *IEEE Trans. Power Electron.*, vol. 37, no. 10, pp. 12502–12512, May 2022.

[8] F. Chai, Y. Li, Y. Pei, and Z. Li, "Accurate modelling and modal analysis of stator system in permanent magnet synchronous motor with concentrated winding for vibration prediction," *IET Electr. Power Appl.*, vol. 12, no. 8, pp. 1225–1232, Sep. 2018.

[9] D. Kim, M. Park, J. Sim, and J. Hong, "Advanced method of selecting number of poles and slots for low-frequency vibration reduction of traction motor for elevator," *IEEE/ASME Trans. Mechatronics*, vol. 22, no. 4, pp. 1554–1562, Aug. 2017.

[10] S. G. Min and B. Sarlioglu, "Investigation of electromagnetic noise on pole and slot number combinations with possible fractional-slot concentrated windings," in *Proc. IEEE Transport. Electrific. Conf. Expo (ITEC)*, Jun. 2017, pp. 241–246.

[11] H. Lan, J. Zou, Y. Xu, and M. Liu, "Effect of local tangential force on vibration performance in fractional-slot concentrated winding permanent magnet synchronous machines," *IEEE Trans. Energy Convers.*, vol. 34, no. 2, pp. 1082–1093, Jun. 2019.

[12] H. Fang, D. Li, R. Qu, and P. Yan, "Modulation effect of slotted structure on vibration response in electrical machines," *IEEE Trans. Ind. Electron.*, vol. 66, no. 4, pp. 2998–3007, Apr. 2019.

[13] Q. Chen, G. Xu, F. Zhai, and G. Liu, "A novel spoke-type PM motor with auxiliary salient poles for low torque pulsation," *IEEE Trans. Ind. Electron.*, vol. 67, no. 6, pp. 4762–4773, Jun. 2020.

[14] Y. Mao, W. Zhao, S. Zhu, Q. Chen, and J. Ji, "Vibration investigation of spoke-type PM machine with asymmetric rotor considering modulation effect of stator teeth," *IEEE Trans. Ind. Electron.*, vol. 68, no. 10, pp. 9092–9103, Oct. 2021.

[15] S. Zhu, W. Zhao, J. Ji, G. Liu, Y. Mao, and T. Liu, "Investigation of bread-loaf magnet on vibration performance in FSCW PMSM considering force modulation effect," *IEEE Trans. Transport. Electrific.*, vol. 7, no. 3, pp. 1379–1389, Sep. 2021.

[16] Z. Li, J. Xia, Z. Guo, B. Lu, and G. Ma, "Reduction of pole-frequency vibration of surface-mounted permanent magnet synchronous machines with piecewise stagger trapezoidal poles," *IEEE Trans. Transport. Electrific.*, vol. 9, no. 1, pp. 833–844, Mar. 2023.

[17] Z. Li, J. Xia, Z. Guo, B. Lu, and G. Ma, "Analysis and reduction of pole-frequency vibration of surface mounted permanent magnet synchronous machines with fractional slot concentrated winding considering the radial and tangential forces," *IEEE Trans. Transport. Electrific.*, vol. 9, no. 2, pp. 2129–2140, Nov. 2022.

[18] S. Zhu, W. Zhao, J. Ji, G. Liu, and C. H. T. Lee, "Design to reduce modulated vibration in fractional-slot concentrated-windings PM machines considering slot–pole combination," *IEEE Trans. Transport. Electrific.*, vol. 9, no. 1, pp. 575–585, Mar. 2023.

[19] J. Kim, S. Park, J. Ryu, and M. Lim, "Comparative study of vibration on 10-pole 12-slot and 14-pole 12-slot PMSM considering tooth modulation effect," *IEEE Trans. Ind. Electron.*, vol. 70, no. 4, pp. 4007–4017, Apr. 2023.

[20] J. Hong, S. Wang, Y. Sun, and H. Cao, "A high-precision analytical method for vibration calculation of slotted motor based on tooth modeling," *IEEE Trans. Ind. Appl.*, vol. 57, no. 4, pp. 3678–3686, Jul. 2021, doi: 10.1109/TIA.2021.3080231.

[21] M. Wang, J. Zhu, L. Guo, J. Wu, and Y. Shen, "Analytical calculation of complex relative permeance function and magnetic field in slotted permanent magnet synchronous machines," *IEEE Trans. Magn.*, vol. 57, no. 3, pp. 1–9, Mar. 2021.

[22] J.-H. Kim et al., "Investigation on radial vibration of FSCW PMSM according to pole/slot combination considering phase of radial, tangential force and moment," *IEEE Trans. Ind. Appl.*, vol. 60, no. 1, pp. 439–449, Oct. 2024.

[23] M.-R. Park, J.-W. Jung, D.-Y. Kim, J.-P. Hong, and M.-S. Lim, "Design of high torque density multi-core concentrated flux-type synchronous motors considering vibration characteristics," *IEEE Trans. Ind. Appl.*, vol. 55, no. 2, pp. 1351–1359, Mar. 2019, doi: 10.1109/TIA.2018.2876329.

[24] J. -W. Jung, J. -P. Hong, and Y. -K. Kim, "Characteristic analysis and comparison of IPMSM for HEV according to pole and slot combination," in *Proc. IEEE Vehicle Power Propuls. Conf.*, Jun. 2007, pp. 778–783.

[25] S.-G. Lee, S. Kim, J.-C. Park, M.-R. Park, T. H. Lee, and M.-S. Lim, "Robust design optimization of SPMSM for robotic actuator considering assembly imperfection of segmented stator core," *IEEE Trans. Energy Convers.*, vol. 35, no. 4, pp. 2076–2085, Dec. 2020.

Jae-Hyun Kim (Member, IEEE) received the bachelor's degree in mechanical engineering and the Ph.D. degree in automotive engineering from Hanyang University, Seoul, South Korea, in 2017 and 2023, respectively.

From 2023 to 2024, he was with Research and Development Division, Hyundai Mobis, Uiwang, South Korea. Since 2024, he has been with the Department of Mechanical Engineering, Yeungnam University, Gyeongsan, South Korea, as an Assistant Professor. His research interests include the design and analysis of vibration and noise of electric machines.

Yun-Jae Won received the bachelor's degree in automotive engineering from Hanyang University, Seoul, South Korea, in 2021, where he is currently pursuing the Ph.D. degree in automotive engineering.

His research interests include the design and vibration and noise of electric machines.

Myung-Seop Lim (Senior Member, IEEE) received the bachelor's degree in mechanical engineering and the master's and Ph.D. degrees in automotive engineering from Hanyang University, Seoul, South Korea, in 2012, 2014, and 2017, respectively.

From 2017 to 2018, he was a Research Engineer with Hyundai Mobis, Yongin, South Korea. From 2018 to 2019, he was an Assistant Professor with Yeungnam University, Daegu, South Korea. Since 2019, he has been with Hanyang University, where he is currently an Assistant Professor. His research interests include electromagnetic field analysis and electric machinery for mechatronics systems, such as automotive and robot applications.